The signature of shear-induced anisotropy in granular media

Ning Guo, Jidong Zhao *

Department of Civil and Environmental Engineering, Hong Kong University of Science and Technology, Clearwater Bay, Kowloon, Hong Kong

ABSTRACT

This paper presents a micro-mechanical study on the characteristics of shear-induced anisotropy in granular media. Based on three-dimensional Discrete Element Method (DEM) simulations, the distinct features associated with the evolution of internal granular structure and different anisotropy sources during drained/undrained shearing of granular samples are carefully examined. The study finds that *static liquefaction* occurs when the geometrical anisotropy in a sample dominates the mechanical anisotropy in the overall shear strength, and the weak force network features an exceptionally high proportion of sliding contacts and develops certain degree of anisotropy. *Phase transformation* corresponds to a transitional, unstable state associated with a dramatic change in both coordination number and the proportion of sliding contacts in all contacts. The *critical state* in a granular material is always associated with a highly anisotropic fabric structure wherein both the critical void ratio and critical fabric anisotropy are uniquely related to the mean effective stress. The relations provide a more comprehensive definition for the critical state in granular media with proper reference to the critical fabric anisotropy.

© 2012 Elsevier Ltd. All rights reserved.

1. Introduction

Granular media are important to our everyday life. Granular sand plays a key role in many infrastructures pertaining to the quality and safety of our daily life, including water dams, residential buildings, bridges, motorways, engineered slopes, embankments and foundations. The behaviour of granular media, however, remains far from well understood for researchers in many disciplines. Of particular interest in recent granular mechanics research is the anisotropic behaviour of a granular medium when subjected to shearing. Anisotropy reflects not only the soil fabric composition in connection to the spatial arrangement of soil particles, voids and interparticle contacts but also the changes of these microstructures induced by applied loads [35,8,32]. Both experimental and theoretical studies have suggested that fabric anisotropy and its evolution during granular soil shearing contribute to key aspects of the macroscopic sand responses, including dilatancy, non-coaxiality and shear strength [44,20,11]. One of the focused areas of current granular material research has been identifying the role of fabric anisotropy and including its influence in constitutive modelling [29,25,16,26,14,15]. As Radjaï et al. [41] and Radjaï [40] indicate, a complex macroscopic behaviour like anisotropy involves nontrivial details of the underlying microstructures. Without effective tools to identify the microstructural

origin of fabric anisotropy and its evolution, it is difficult for phenomenological models to provide faithful reflections of and reasonable explanations for the microstructural changes associated with various important macroscopic phenomena.

Micromechanics-based approaches, particularly those based on the Discrete Element Method (DEM), have proven useful [44,50,42,24,48,52,2,51,27,28]. In this paper, we employ a three-dimensional DEM to explore the characteristics of shear-induced anisotropy and its evolution during typical granular media shearing processes. We focus on three characteristic states that are important in soil mechanics: *liquefaction*, *phase transformation* and the *critical state*. They represent typical deformation stages in a granular material and have both theoretical significance and practical importance. Interestingly, all three states correspond to zero-dilatancy in granular materials, but they point to entirely different underlying mechanisms which are considered closely related to anisotropy [26,58]. This paper is devoted to exploring important properties of anisotropy identifiable for each characteristic state to provide useful references for future constitutive modeling on granular soils.

The paper is organised as follows. Section 2 describes the methodology and quantity definitions used in later sections. Section 3 presents the main results on macroscopic responses, the evolution of internal structures and anisotropy, and observations and discussion on the chosen three characteristic states. The last section provides the major conclusions of the study and some further discussion.

---

* Corresponding author. Fax: +852 2358 1534.
  E-mail address: jzhao@ust.hk (J. Zhao).

2. Approach and formulation

A three-dimensional Discrete Element Method code, ESyS-Particle, has been modified for the present study [1,54,19]. A linear force–displacement contact law for spherical particles is employed where two elastic moduli must be specified to describe the contact behaviour between contacted particles, normal stiffness k_n and tangential stiffness k_s. Goldenberg and Goldhirsch [18] have suggested that the value of k_s/k_n for realistic granular materials should be around $2/3 < k_s/k_n < 1$, which correlates well with the Cattaneo–Mindlin model [23] for elastic sphere contact. We assume $k_n/r = k_s/r = 100$ MPa, where r is the particle radius. The interparticle sliding is assumed to be governed by Coulomb's friction law, which adopts a sliding frictional coefficient $\mu = 0.5$. Following a common particle rotation assumption (e.g., Itasca PFC3D), each particle in a granular system is considered freely rotatable: a particle rolling is a direct consequence of inter-particle friction, and the angular velocity of the particle is updated by the moments calculated from the frictional forces applied to the particle surface. Considering non-spherical particles and/or interparticle rolling resistance may help produce more realistic granular particle behaviours, but will not be pursued here to avoid excessive complication.

2.1. Sample packing and solution procedures

A cubic packing of polydisperse spherical particles is considered. Inside a cubic box confined by six rigid frictionless walls, 31,769 total particles with radii ranging from 0.2 mm to 0.6 mm are randomly generated. In real, natural granular materials like sand, a log-normal distribution may be more realistic to describe the size distribution. Using overly fine particles mixed with coarse ones in a DEM simulation, however, could potentially cause problems, such as segregation during loading or numerical difficulties. A power law is thus employed as a good approximation of the log-normal distribution by truncating the range of excessively small particles. Fig. 1 shows the actual distribution with an exponent $D = 3.63$ in the power law, where D is called the *fractal dimension* [30].

After the desired number of particles is generated in the cubic box, the packing is then isotropically consolidated, and the consolidation is accomplished in two stages. In the first stage, the confining pressure is gradually increased to 90% of the desired stress level. To generate packings with different initial void ratios, different frictional coefficients μ are employed. Upon finishing the first stage, μ is fixed at 0.5. The consolidation process is then continued
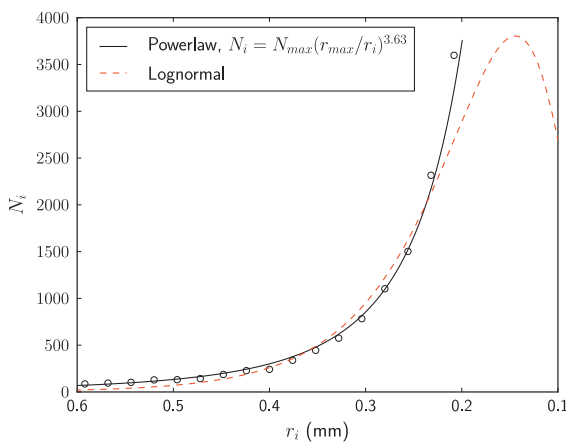

Fig. 1. The size distribution of particles used for cubic packing. N_i is the number of particles with a radius of r_i, and N_{max} denotes the total number of particles with a maximum radius r_{max} in the packing.

Table 1
Sample packings to be sheared under drained and undrained conditions.

Series	Sample	e_0	Description
Series I	UL	0.644	Undrained shear on loose sample
	UM	0.634	Undrained shear on medium dense sample
	UD	0.612	Undrained shear on dense sample
Series II	DL	0.645	Drained shear on loose sample
	DM	0.621	Drained shear on medium dense sample
	DD	0.539	Drained shear on dense sample

by increasing the confining pressure to the final value, $p_0' \approx 190\ kPa$. After the two-staged isotropic consolidation, the packings obtained with different void ratios are ready for shear.

The shearing on each sample is performed in two different loading conditions commonly encountered in soil mechanics: undrained and drained. As our DEM only involves dry particles, the undrained condition is only simulated approximately, e.g., by imposing a constant volume constraint on the sheared sample (see also [56,6]). During shearing, the horizontal strain is continuously adjusted with the vertical compression to maintain a constant value for the total assembly volume. For the drained shear tests, conversely, the horizontal pressure is kept constant during the entire compression. Table 1 summarises relevant information about six packings used for 2 shear test series. Series I involves undrained tests on three packings, UL, UM and UD, which differ from one another in initial void ratio and typically can be used to represent sand in very loose, medium-dense and dense states, respectively. Likewise, three packings are prepared for drained tests in series II. In Table 1, e_0 is the initial void ratio of a sample before shear.

2.2. Macroscopic variable definitions

We first define several quantities, including stress, strain and anisotropy, based on a discrete description of DEM.

2.2.1. Stress tensor and strain tensor

We follow the stress tensor definition proposed by Christoffersen et al. [10]:

$$\sigma_{ij} = \frac{1}{V} \sum_{c \in N_c} f_i^c d_j^c, \tag{1}$$

where V is the total volume of the assembly, N_c is the total number of contacts, $\vec{f}^c$ is the contact force at a contact and $\vec{d}^c$ is the branch vector joining the centres of two contacting particles. Using Eq. (1), we can derive the mean effective and deviatoric stresses commonly used in soil mechanics:

$$p' = \frac{1}{3}\sigma_{ii}, \quad q = \sqrt{\frac{3}{2}\sigma_{ij}'\sigma_{ij}'}, \tag{2}$$

where σ_{ij}' is the deviatoric part of the stress tensor σ_{ij}.

A strain tensor should ideally also be derived from the available microscopic information [5]. In this study, however, the strain is only used as a rough indicator of the shear deformation level for a sample and thus does not require an accurate definition here. A specific definition of strain tensor for a cubic sample under triaxial compression is assumed, according to the displacement gradient at the boundary walls, e.g., $\epsilon_{ij} = \partial u_i / \partial x_j$ (the expression is automatically symmetric under triaxial conditions). The axial strain ϵ_1 and volumetric strain ϵ_v at a certain deformation stage, which are relevant quantities for our study, can be defined thus:

$$\epsilon_1 = \ln\frac{H_0}{H}, \quad \epsilon_v = \epsilon_1 + \epsilon_2 + \epsilon_3 = \ln\frac{V_0}{V}, \tag{3}$$

where H_0 and V_0 are, respectively, the initial height and volume of the assembly before shearing and H and V are their current values at the instant of calculation. Compression is taken as positive in this paper.

2.2.2. Geometrical and mechanical anisotropy

In quantifying anisotropy in a granular assembly, two anisotropy sources are distinguished: *geometrical anisotropy* and *mechanical anisotropy* [8]. Geometrical anisotropy is defined as the local orientation of a contact plane that gives rise to the global anisotropic phenomenon. Mechanical anisotropy is mainly caused by external forces and depends on the induced contact forces in relation to contact plane orientations. For an assembly of polydisperse spherical particles, geometrical anisotropy can be expressed using the distribution of *contact normals* and *branch vectors*. The definition of *fabric tensor* proposed by Satake [46] and Oda [36] is used here to quantify the *contact normal* orientation.

$$\phi_{ij} = \int_{\Theta} E(\Theta) n_i n_j \, d\Theta = \frac{1}{N_c} \sum_{c \in N_c} n_i n_j, \tag{4}$$

where $\vec{n}$ is the unit vector along the normal direction of the contact plane, Θ characterises the orientation of $\vec{n}$ relative to the global coordination system and $E(\Theta)$ is the distribution probability function. In most cases, it suffices to employ a second-order Fourier expansion of $E(\Theta)$ to characterise the contact normals [39,47]:

$$E(\Theta) = \frac{1}{4\pi} \left[1 + a_{ij}^c n_i n_j \right], \tag{5}$$

where the second-order anisotropy tensor a_{ij}^c is deviatoric and symmetric and characterises the fabric anisotropy. After substituting Eq. (5) into Eq. (4) and performing the integration, one has

$$a_{ij}^c = 15/2 \; \phi_{ij}', \tag{6}$$

where ϕ_{ij}' is the deviatoric part of ϕ_{ij}.

Branch vectors may also constitute an important part of geometrical anisotropy, especially when the granular assembly comprises polydisperse or non-spherical particles. In essence, the branch vector distribution can be expressed similarly to the contact normals in Eqs. (4) and (5) [37]

$$d_{ij} = \frac{1}{4\pi} \int_{\Theta} \bar{d}(\Theta) n_i n_j \, d\Theta = \frac{1}{N_c} \sum_{c \in N_c} \frac{d^c n_i n_j}{1 + a_{kl}^c n_k n_l} \tag{7a}$$

$$\bar{d}(\Theta) = \bar{d}^0 \left[1 + a_{ij}^d n_i n_j \right], \tag{7b}$$

where

$$a_{ij}^d = \frac{15}{2} \frac{d_{ij}'}{\bar{d}^0}$$

is the geometrical anisotropy relevant to the branch vectors. a_{ij}^d has the same property as a_{ij}^c. $\bar{d}^0 = d_{ii}$ is the average branch vector length calculated over different Θ and may differ from $\bar{d}$, which is averaged over all contacts. In the polydisperse spherical assemblies considered in this paper, branch vectors have only normal components.

The mechanical anisotropy can be split into normal force anisotropy (caused by normal contact forces) and tangential force anisotropy (induced by tangential contact forces), which are respectively defined as follows [47]:

$$\chi_{ij}^n = \frac{1}{4\pi} \int_{\Theta} \bar{f}^n(\Theta) n_i n_j \, d\Theta = \frac{1}{N_c} \sum_{c \in N_c} \frac{f^n n_i n_j}{1 + a_{kl}^c n_k n_l} \tag{8a}$$

$$\bar{f}^n(\Theta) = \bar{f}^0 \left[1 + a_{ij}^n n_i n_j \right], \tag{8b}$$

and

$$\chi_{ij}^t = \frac{1}{4\pi} \int_{\Theta} \bar{f}^t(\Theta) t_i n_j \, d\Theta = \frac{1}{N_c} \sum_{c \in N_c} \frac{f^t t_i n_j}{1 + a_{kl}^c n_k n_l} \tag{9a}$$

$$\bar{f}_i^t(\Theta) = \bar{f}^0 \left[a_{ik}^t n_k - (a_{kl}^t n_k n_l) n_i \right], \tag{9b}$$

where

$$a_{ij}^n = \frac{15}{2} \frac{\chi_{ij}^m}{\bar{f}^0}, \qquad a_{ij}^t = \frac{15}{3} \frac{\chi_{ij}'^t}{\bar{f}^0}$$

Similar to the previous cases, $\bar{f}^0 = \chi_{ii}^n$ is the average normal force calculated over different Θ and may differ from the average normal force $\bar{f}$ over all contacts.

The various definitions outlined above show that each of the four anisotropy tensors, a_{ij}^c, a_{ij}^d, a_{ij}^n and a_{ij}^t, can be conveniently used to characterise the anisotropic behaviour originating from a distinct source. Because all four tensors are deviatoric in nature, it is convenient to use their deviatoric invariants to quantify the degree of anisotropy in each case.

$$a_* = \text{sign}(S_r) \sqrt{\frac{3}{2} a_{ij}^* a_{ij}^*}, \tag{10}$$

where the sub/super-script $*$ stands for c, d, n or t, corresponding to one of the four cases of anisotropy mentioned above, respectively. S_r is a normalised quantity of the double contraction of a_{ij}^* and σ_{ij}' defined below:

$$S_r = \frac{a_{ij}^* \sigma_{ij}'}{\sqrt{a_{kl}^* a_{kl}^*} \sqrt{\sigma_{mn}' \sigma_{mn}'}} \tag{11}$$

The sign (S_r) in Eq. (10) signifies the relative orientation of the principal direction of a_{ij}^* with respect to that of the stress tensor. A positive sign of a_* thus indicates that the major principal direction of a_{ij}^* is closer (e.g., within $\arccos(\sqrt{3}/3)$ for an axisymmetric case, as shown in Fig. 2), to the major principal direction of the stress tensor,
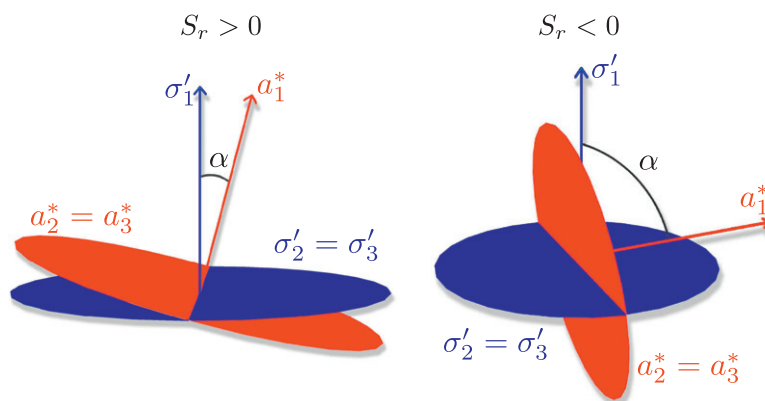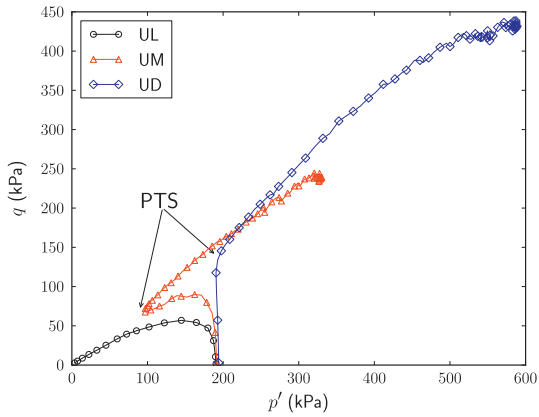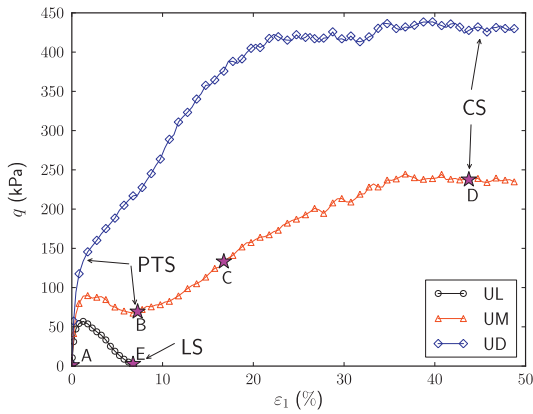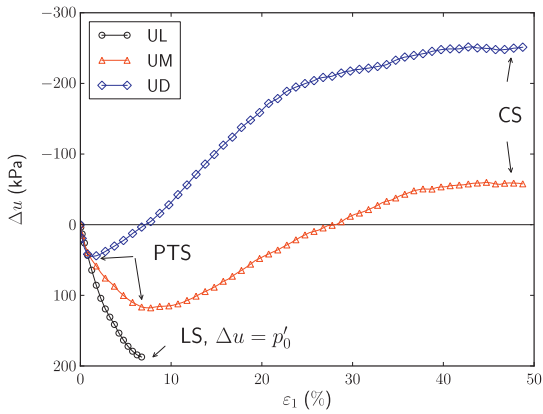

Fig. 2. Illustration of sign (S_r) with the relative stress and fabric tensor orientations.

(a) Loading path

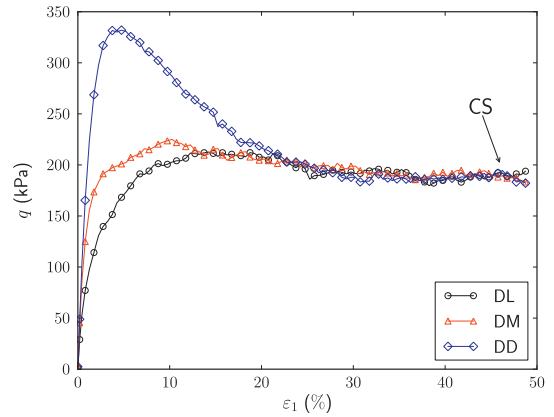(b) Deviatoric stress vs. axial strain

(c) Pseudo excess pore water pressure
vs. aaxial strain

Fig. 3. Mechanical responses of samples subjected to undrained shear in Test Series I. PTS: phase transformation state; LS: liquefaction state; CS: critical state.

and a negative sign for a_* otherwise. S_r itself can be used to indicate the coaxiality between the stress tensor and a specific anisotropic tensor, e.g., $S_r = 1$ denotes the coaxiality of the two. Ouadfel and Rothenburg [39] have employed a similar definition.

3. Results and analyses

In this section, we (a) examine the macroscopic stress–strain and volumetric responses of different packings under shearing; (b) visualise and analyse the change of internal structures during

(a) Deviatoric stress vs. axial strain
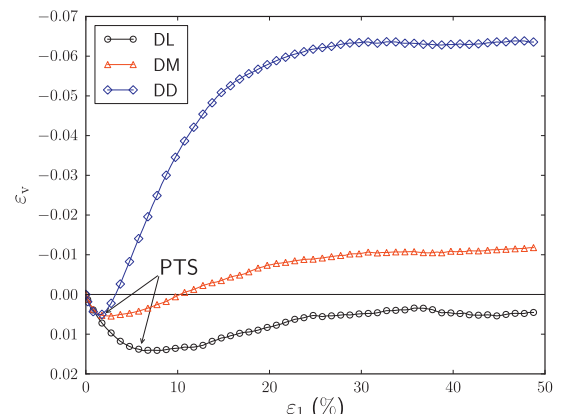
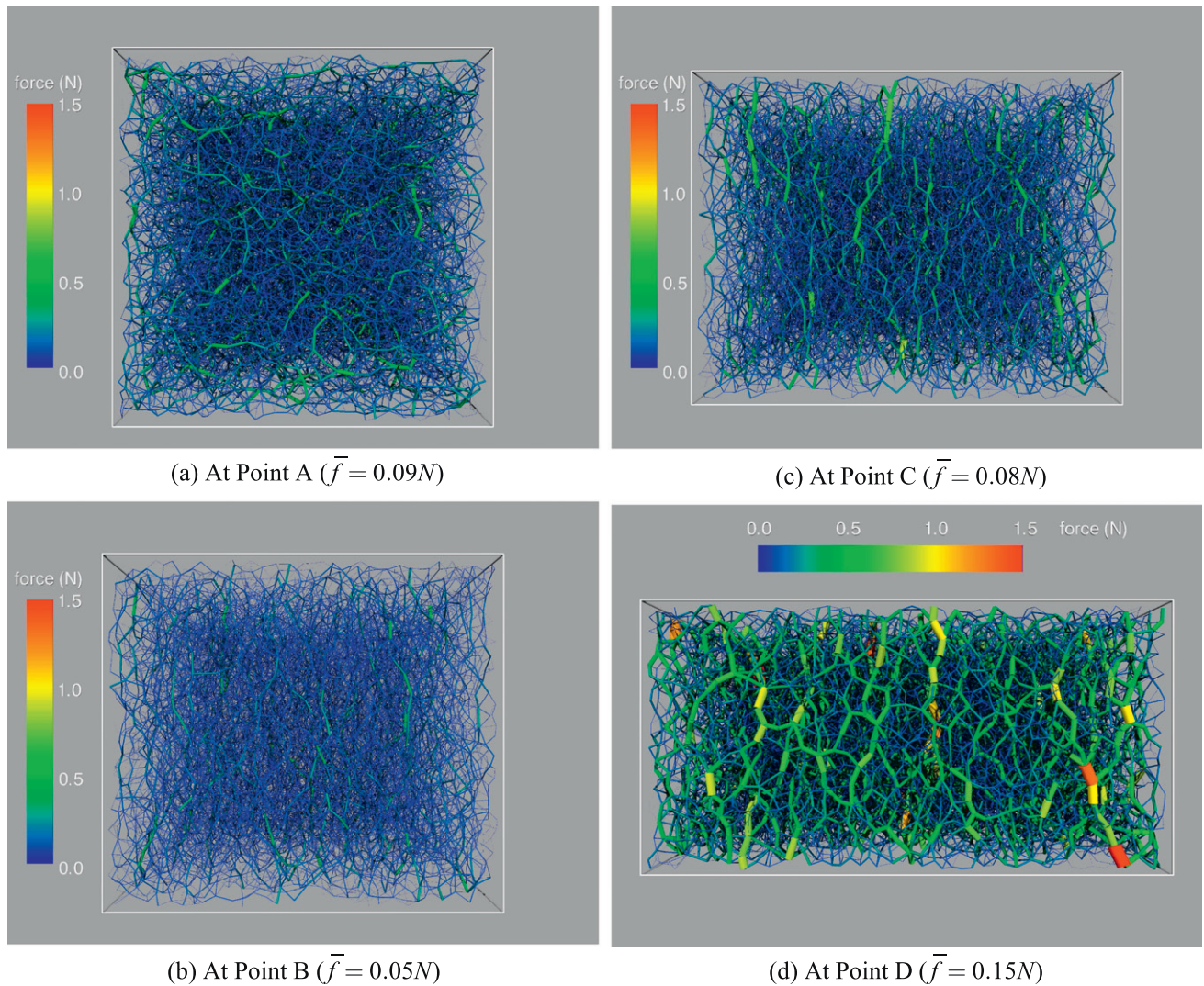(b) Volumetric strain vs. axial strain

Fig. 4. Material responses for samples under drained shear in Series II.

different deformation stages via a contact force network; (c) quantify the anisotropy and its evolution during shearing; and (d) investigate the signatures associated with the three characteristic states.

3.1. Macroscopic responses for different packings under shearing

To explore anisotropic behaviour at a critical state, all samples are sheared to a relatively large deformation (e.g., around 50% of axial strain) unless prevented by liquefaction. At 50% of axial strain, we find that all characteristic critical state conditions defined in classic critical state theory are approximately satisfied, i.e., a sample is typically observed to experience continuous flow with constant volume (or constant pore pressure) with a stagnated stress ratio. No shear banding localisation has been observed in our simulations, most likely because the study uses rigid boundary walls. Fig. 3 shows the mechanical responses of different samples for Series I, and Fig. 4 shows those for Series II. In the undrained case, the total confining pressure σ_3 is assumed to be constant such that the *pseudo* excess pore water pressure Δu for a dry packing can be calculated by the difference between σ_3 and the mean effective stress p' defined in Eq. (2). Δu is employed here to help identify the various characteristic states for the undrained tests.

Fig. 3 shows the simulated results for the three samples in Series I. Under undrained shearing, a dense sample (UD) appears to be predominantly dilative after an initial instantaneous contraction, which is reflected in the development of pseudo excess pore pressure presented in Fig. 3c. For the medium dense sample (UM), the initial contractive trend is so intense that a significant amount of

(a) At Point A ($\bar{f} = 0.09N$)

(c) At Point C ($\bar{f} = 0.08N$)

(b) At Point B ($\bar{f} = 0.05N$)

(d) At Point D ($\bar{f} = 0.15N$)

Fig. 5. Evolution of force chain network and typical internal structure during UM shearing. (a) At Point A (Fig. 3b) ($\epsilon_1 = 0.0\%$); (b) At Point B (PTS) ($\epsilon_1 = 7.25\%$); (c) At Point C ($\epsilon_1 = 16.75\%$); (d) At the critical state Point D ($\epsilon_1 = 43.75\%$).

excess pore pressure is generated, which considerably reduces the effective stress and shear strength. It later manages to re-mobilise its friction to pull the sample response back to dilation. Consequently, an obvious turning point is observed in the loading path in Fig. 3a, which marks the 'Phase Transformation State' (PTS) for the sample. Conversely, the loose sample (UL) demonstrates a steady contraction response such that the excess pore pressure continues to build up until, at an axial strain of 7%, it totally cancels out the total stress and causes a vanishingly small effective stress. At this point, the static liquefaction state is reached. These observations compare qualitatively favourably with typical experimental results, including those reported by Yoshimine et al. [57] and summarised by Mitchell and Soga [32].

Fig. 4 shows the simulated results for Series II. Similar trends are observed in which dense samples tend to be more dilative while loose samples are more contractive. No liquefaction occurs for the loose case due to the drainage conditions. The medium dense sample also displays an appreciable initial contraction followed by dilation. This series of tests has also captured the transition point of volumetric change, or PTS, and the critical state at around 50% of axial strain.

Summary 1. The chosen packings and tests in Series I and II reproduce the representative soil responses observed in the laboratory. The characteristics states we wish to investigate are identifiable in these tests.

3.2. Internal structure evolution at different loading stages

It is interesting to visualise the change in microstructural heterogeneity of a granular sample during the shearing process. The observation may help us analyse the physical mechanisms at different deformation stages for a material. A granular system is known to transmit forces through an interparticle contact force network [31]. The network reflects both the interparticle fabric connection and how the fabric transmits the external load within the granular system. Radjaï et al. [42] and others have identified an interesting bimodal character of force transmission in the contact force network, which is indeed an important characteristic of a network under deviatoric shear. The contact force network is ideal for us to study the internal structure characteristics. Consider the UM case as an example. Fig. 5 shows the contact force network changes at four strain levels of UM, A, B, C and D, as marked in Fig. 3b. Each colourful column in the figures connects the centroids of two contacted particles, and its thickness (or colour) denotes the magnitude of the contact normal force. The following features are observed from the networks at the four states.

Point A: As shown in Fig. 5a, though the sample has not received any shearing at Point A, the distinction between the strong (thick green[1] columns) and weak (thin blue lines) force networks is observable. Because all force chains are randomly oriented, however, the whole network is isotropic to an overall view. The average contact force $\bar{f}$ in the network is around 0.09 N.

Point B: With the increase in shear, the initially randomly oriented strong force chains gradually change their preferential direction to align to the vertical direction. Fig. 5b shows the network developed at Point B when a 7.25% axial strain has been developed. The point corresponds to the phase transformation state for UM. The weak force network at Point B remains largely isotropic, while the strong network finds a preferred vertical (shearing direction) orientation. Compared to Point A, the entire network at Point B appears to be weakened considerably, with an average contact force of $\bar{f} = 0.05$ N. The steady contraction of the relative loose UM sample between Points A and B may contribute to the drop of its overall strength.

Point C: With a higher strain level (16.75% axial strain) at Point C, the force network, as in Fig. 5c, demonstrates a much clearer anisotropic nature. While the weak force network stays roughly isotropic, the vertically oriented strong force chains become much thicker than those in Fig. 5b, and the average contact force also increases to $\bar{f} = 0.08$ N. The greatest contact force at Point C is twice that at Point B.

Point D: The UM packing reaches the critical state at this point. The entire network is dominated by the thick, vertically penetrating strong force chains, as in Fig. 5d. The greatest contact force at Point D is approximately two times that at Point C. The average contact force at D is around 0.15 N, the highest of all four states. The weak force network remains isotropic at the critical state.

Summary 2. The internal structure in a granular system evolves continuously in its contact force network as shear deformation develops. A weak network always shows an isotropic feature at all strain levels, while the strong contact force network dominates the nature of the whole network. A strongly anisotropic strong network always leads to an anisotropic internal structure for the entire sample. This observation confirms the bimodal theory by Radjaï et al. [42]. The critical state in granular sand indicates a clearly anisotropic fabric structure.

Remark 1. Contact force chains, particularly strong ones, depict an appreciable spatial correlation, as observed in Fig. 5. Experiments on dense photoelastic disk assembly by Majmudar and Behringer [31] indicate a persisting spatial correlation in the force chain direction of approximately 15 particle diameters. The weak force network has only a couple of particle diameters of correlation. Their observation was based on monosized granular systems. How the grain size distribution, initial density and/or loading paths affect the spatial correlation are interesting topics for future study.

3.3. Correlation between anisotropy and shear strength

The observations on UM in Figs. 5 and 3b indicate a proportional relation between the anisotropy and shear strength in one sample. UM at Point D has a much stronger anisotropic network and higher shear strength. Rothenburg et al. [43] and Rothenburg and Bathurst [44] have established an analytical correlation between the anisotropy and shear strength, the *stress–force–fabric relationship*, for 2D cases. Chantawarungal [9] has further generalised the relationship for 3D cases in the following form:

$$\sigma_{ij} = \frac{N_c \bar{f} \bar{d}}{3V} \left\{ \delta_{ij} + \frac{2}{5} \left(a_{ij}^c + a_{ij}^n + \frac{3}{2} a_{ij}^t \right) \right.$$
$$\left. + \frac{2}{35} \left[\left(a_{kl}^n - a_{kl}^t \right) a_{kl}^c \delta_{ij} + \left(4a_{il}^n + 3a_{il}^t \right) a_{lj}^c \right] \right\}, \tag{12}$$

where δ_{ij} is the Kronecker delta. Eq. (12) is based on the static force equilibrium of the entire granular body. In his original equation, Chantawarungal [9] has neglected the contribution of the branch vector. As mentioned above, in an assembly containing highly polydisperse particles or particles with nonspherical shapes, the contribution of the branch vector can no long be neglected. Considering a_d, Eq. (12) may be further modified to the following stress–force–fabric relationship using q/p' and the invariants of anisotropy tensors (neglecting the cross products between two anisotropy tensors):

$$\frac{q}{p'} = \frac{2}{5} \left(a_c + a_d + a_n + \frac{3}{2} a_t \right) \tag{13}$$

For a 2D granular system, Voivret et al. [53] have given an expression $q/p' = (a_c + a_d + a_n + a_t)/2$. As Ouadfel and Rothenburg [39] have noted, not all anisotropy sources contribute positively to the shear strength. Considering the non-spherical particle shape leads a_d to negatively contribute to the overall shear strength.

The DEM simulation results in Series I and II have been employed to validate the relationship in Eq. (13), and Fig. 6 presents the correlations. The analytical relationship in Eq. (13) correlates well with the DEM simulations for all tests. Different anisotropy

(a) Undrained condition (Series I)

(b) Drained condition (Series II)
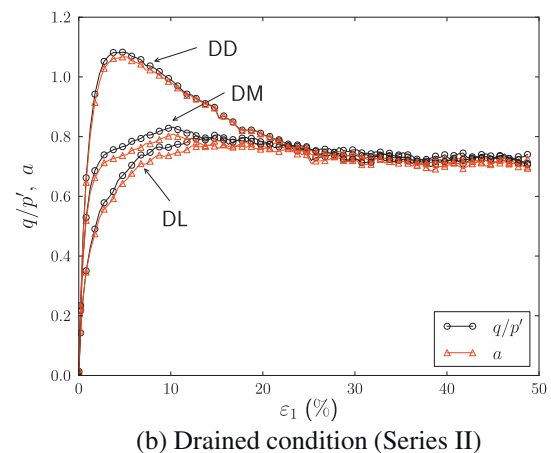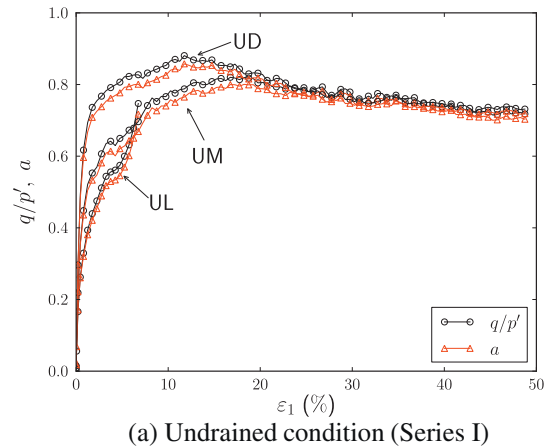
Fig. 6. Verification of the stress-force-fabric relationship in Eq. (13) (q/p') against the DEM simulation of anisotropy ($a = \frac{2}{5}\left(a_c + a_d + a_n + \frac{3}{2} a_t \right)$) for tests in Series I and II.

---

[1] For interpretation of color in Figs. 1–15, the reader is referred to the web version of this article.
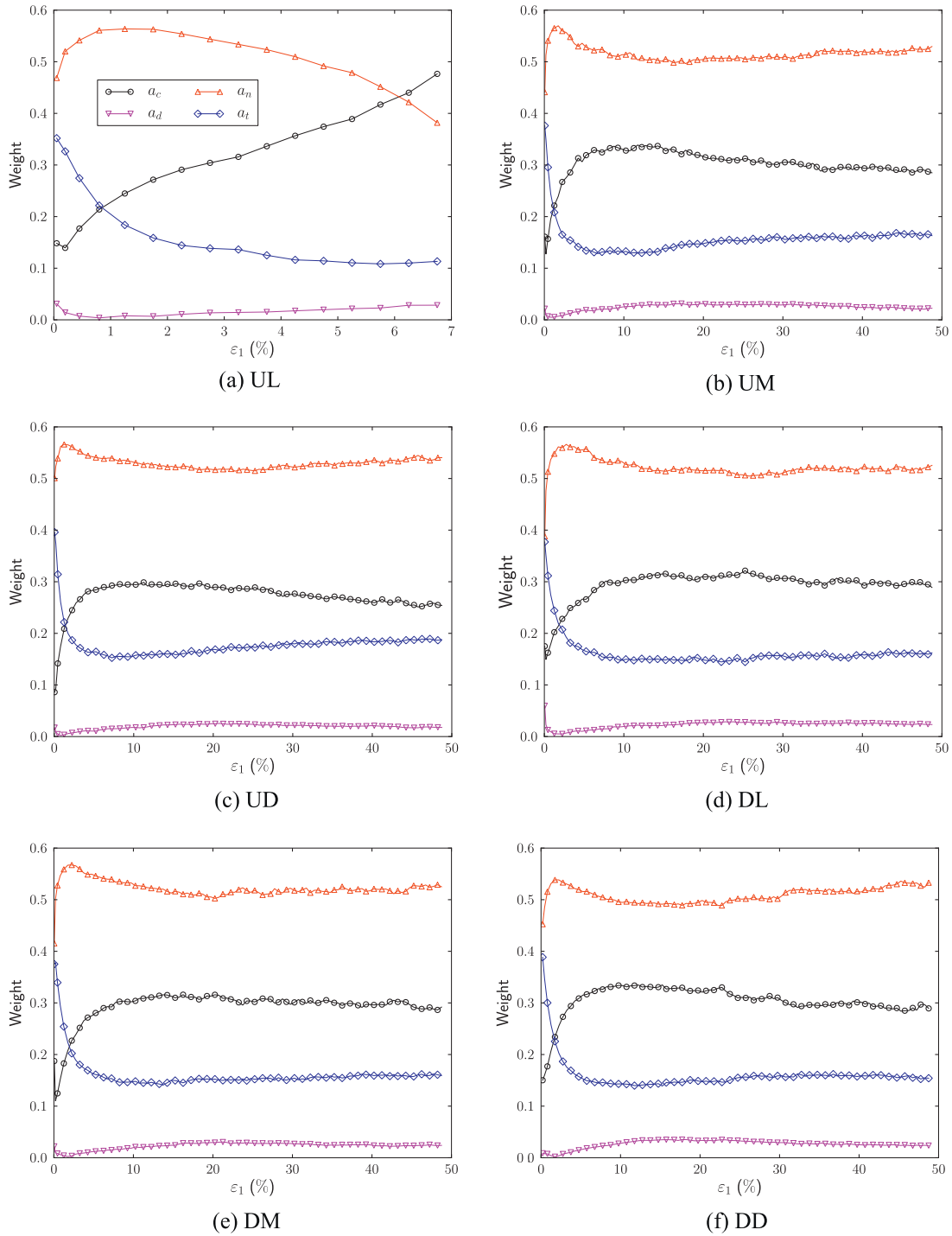
Fig. 7. Contributing weights of different anisotropy sources to the shear strength of samples in Series I and II (including the coefficients in Eq. (13) for each term).

sources may contribute different roles to share the applied shear. It is thus interesting to examine the fraction of the contributions of each anisotropy to the overall shear strength. Fig. 7 presents the relative weights of a_c, a_n, a_t as well as a_d for different tests. Except for UL, the normal contact force anisotropy a_n dominates the overall shear strength by contributing more than 50%, while the contact normal anisotropy a_c plays an important role and contributes approximately 30%. The tangential force anisotropy a_t contributes approximately 18%. In our tests, a_d contributes a negligibly small fraction (only around 2%), obviously due to our use of sphere particles.

Summary 3. The analytical correlation between anisotropy and the shear strength of a granular soil is verified using DEM simulations for both drained and undrained tests. A granular material must develop a certain degree of anisotropy to sustain shearing. Mechanical anisotropy (a_n plus a_t) plays a dominant role in providing shear resistance in medium to dense samples.

3.4. Quantifying anisotropy evolution

Using DEM, it is convenient to quantify the important characteristics of anisotropy and its evolution during the loading process.
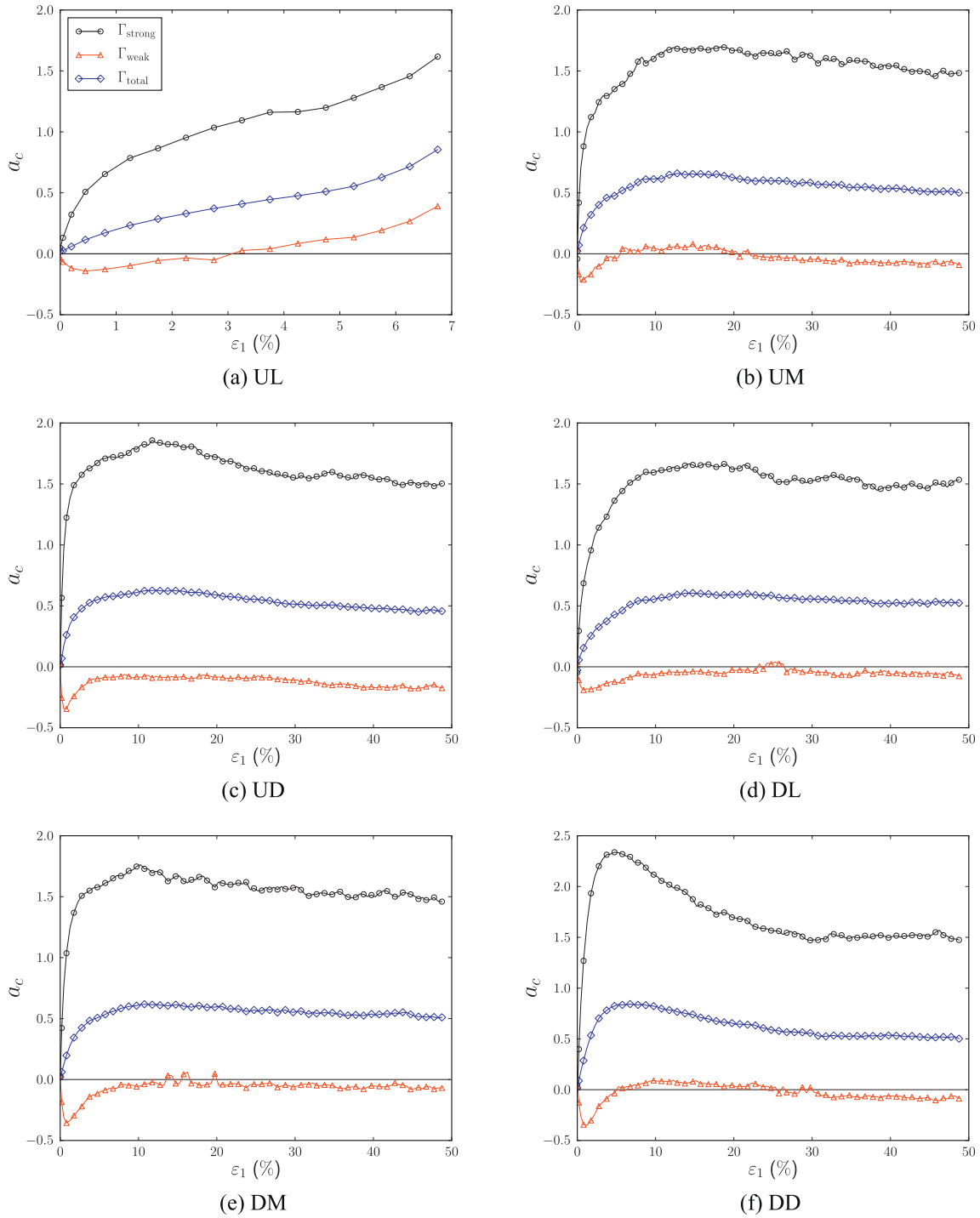
Fig. 8. Evolution of a_c.

We present here the evolution of different anisotropy sources, the coordination number and the proportion of contacts of various natures.

3.4.1. a_c, a_n and a_t

Three anisotropy invariants, a_c, a_n and a_t, are monitored; a_d is neglected here due to its least important role in the sphere particle case. Figs. 8–10 present the results, comparing the contributions from the weak force network (denoted Γ_{weak}), the strong network (denoted Γ_{strong}) and the entire network (denoted Γ_{total}). The

figures provide the following observations for all samples except UL (which is individually discussed in the liquefaction section).

a_c: Fig. 8 presents the following observations, (i) In the weak force network Γ_{weak}, a_c remains negligibly small during the entire loading course. It depicts a quick initial (negative) minimum, increases to a very small value and then remains constant. This indicates that the fabric contacts in the weak force network are statistically isotropic. However, the instantaneous contraction of a sample upon shearing does cause a small degree of anisotropy in the weak network to align perpendicular to the deviatoric stress direction, which implies that a_c is negative. (ii) In the strong force
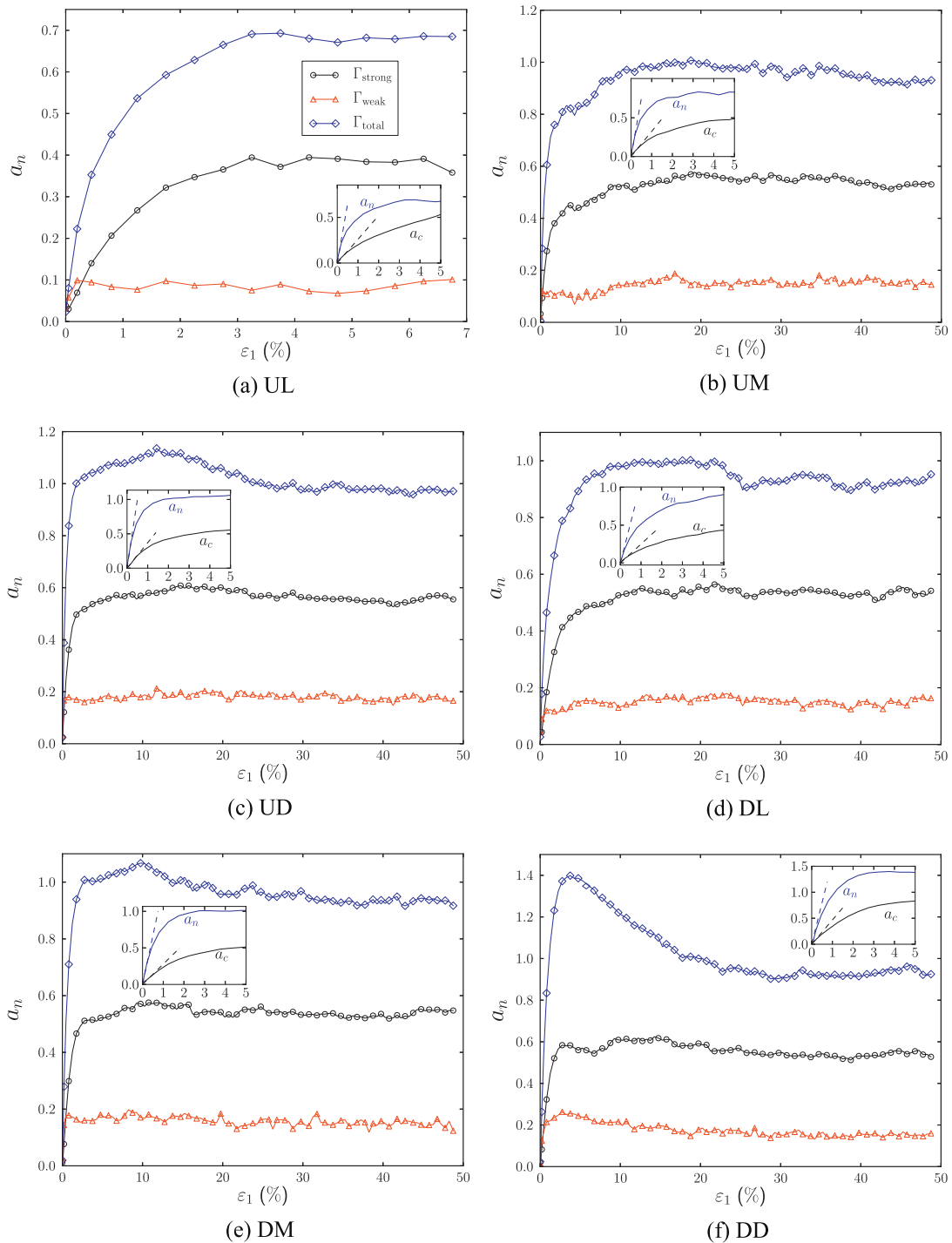
Fig. 9. Evolution of a_n (the insets compare the evolution of a_n with a_c in Γ_{total} at early stage of deformation.)

network, a_c generally increases with strain and reaches a steady critical state value that is at least 7–10 times larger than that in Γ_{weak}. A mild peak is found in UM, UD and DM, while the peak is rather obvious in DD. (iii) In the entire network, a_c follows exactly the same trend as that in Γ_{strong}, with a smaller magnitude due to averaging over all contacts. This again confirms the dominant role played by the strong force network in producing anisotropy.

a_n: The evolution of a_n in Fig. 9 follows a trend largely similar to a_c, though with observable differences. (i) a_n in Γ_{weak} stays at a small positive value during the loading process, which implies that it aligns more in the deviatoric direction. (ii) In Γ_{strong}, a_n is 3 to 4

times greater than that in Γ_{weak}. It evolves to a peak and decreases to the critical state. (iii) In the entire network, the total a_n remains dominated by the strong force subnetwork.[2] An obvious difference between the evolutions of a_n and a_c can be observed from the slope of their curves at the initial deformation stage (see insets in Fig. 9). A relatively large deformation (beyond 5% of axial strain) is required to fully mobilise a_c, while a_n can be mobilised immediately upon the

---

[2] The total a_n is not a simple weighted value of a_n in Γ_{strong} and Γ_{weak}. As such, its value is greater than a_n in either the strong or weak subnetwork, as in Fig. 9, unlike a_c.
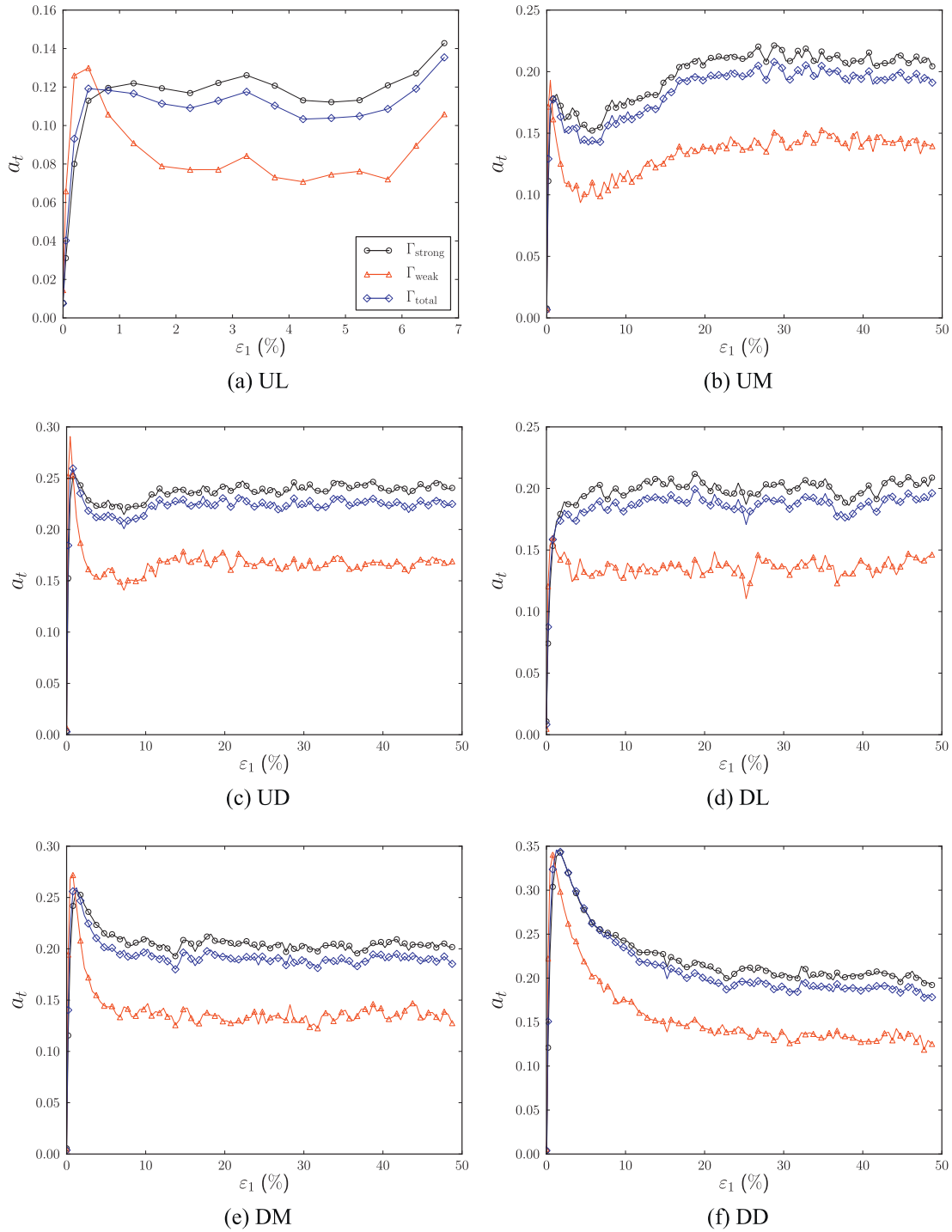
Fig. 10. Evolution of a_t.

imposed shearing and develops to a large value within 0.5% of axial strain.

a_t: As Fig. 10 shows, the tangential force anisotropy a_t is much smaller than a_c and a_n, even in the strong force subnetwork. Upon shearing, the same instantaneous mobilisation is observed for a_t as for a_n. The change is even more dramatic than in a_n. It reaches a peak at a very small strain level (e.g., 1.5%) and steadily decreases with the shearing strain. While it exhibits the same trend in all three networks, a_t in Γ_{strong} and Γ_{total} are close to each other. Greater fluctuations in the evolving a_t curves are observed than

those for a_n and a_c. They may reflect the microscopic 'slip and stick' mode for frictional contact in our DEM simulations [23].

3.4.2. Coordination number and average contact normal force

Fig. 11 shows the evolutions of the average contact normal force $\bar{f}$ and coordination number $Z = 2N_c/N_p$ (N_p is the particle number in contact and N_c is total contact number). Z in all cases but UL develops either a peak or valley at a small strain level and evolves to a steady value. The critical state coordination numbers differ between different samples. $\bar{f}$, however, neither shows an obvious
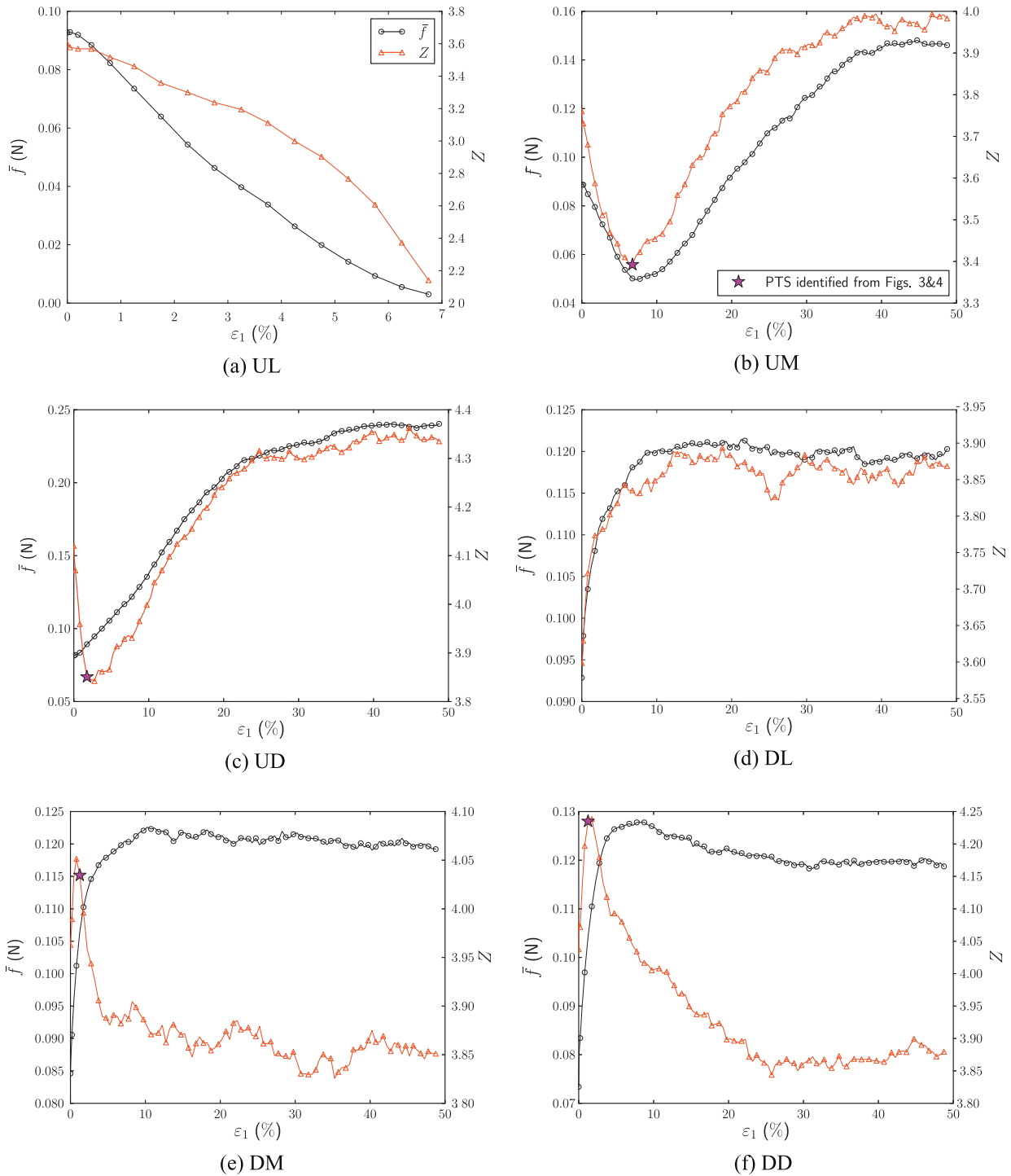
Fig. 11. Evolution of average contact normal force and coordination number of samples in Series I and II.

trend nor correlates well with *Z*. Though not presented here, the evolution of the average tangential contact force follows a similar trend as $\bar{f}$.

3.4.3. Proportions of weak contacts and sliding contacts

It is also interesting to examine the evolution of the proportion of weak force and sliding contacts in the whole contact network for all examples. Figs. 12 and 13 show the results. Again, except UL, all samples follow a similar trend for both quantities. The weak contacts comprise most of the contact network. Its proportion starts from an initial 60% to reach a peak at 63.5–64% and decreases

slightly and stays around 63% at the critical state. In all examples except UL, the sliding contact proportion quickly increases to around 15% and stays there for the entire loading course (UM displays a mild peak before dropping to this value). Alonso-Marroquin et al. [2] have analysed the anisotropic property of the sliding contacts and associated it with soil plasticity.

Summary 4. (1) All three anisotropy sources evolve similarly to shear strain. In each case, the strong force network dominates the overall anisotropy evolution. a_c in the weak network may depict an initial small negative value upon shearing. Mobilising the mechanical anisotropy a_n and a_t is much quicker than mobilising a_c. (2) The
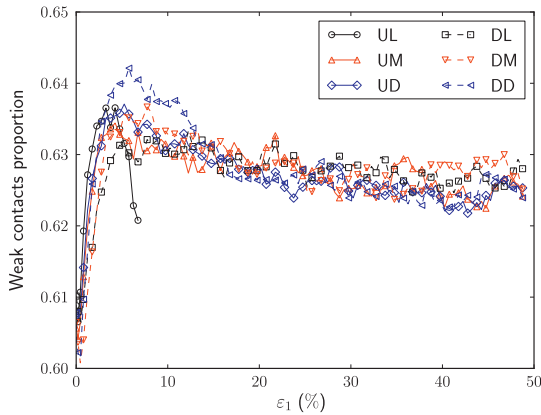
Fig. 12. Evolution of the proportion of weak force contacts in the entire contact network during the loading course.
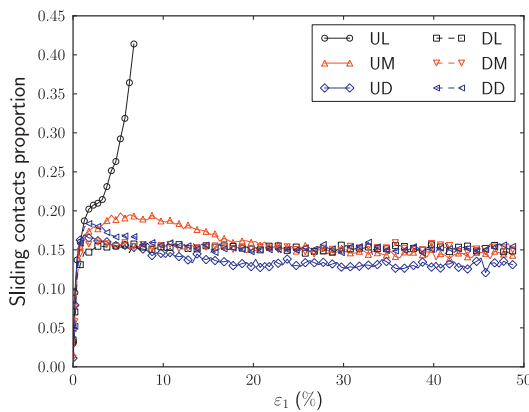

Fig. 13. Proportion of sliding contacts in all contacts for samples in Series I and II.

coordination number quickly reaches a local extremum before evolving to a steady critical state value that is not unique. (3) Weak force contacts contribute a dominant proportion to the entire contact network. Sliding contacts comprise around 1/6 of all contacts during shearing.

Remark 2. A fabric change in a material mainly accommodates the irreversible deformation, which explains why fabric anisotropy a_c is not fully mobilised until a relatively large deformation is developed. In continuum modelling, only plastic deformation drives fabric anisotropy evolution, e.g., $\dot{a}_c \propto f\left(d\varepsilon_{ij}^p\right)$. Upon shearing, establishing fabric contacts quickly renders the fabric tensor coaxial to the deviatoric stress direction (though the fabric magnitude may still be small). Our DEM results for the S_r defined in Eq. (11) confirm this. S_r evolves to unity soon after applying shearing. In a general case (i.e., the presence of initial anisotropy), the evolution law of this S_r may have to be carefully considered, as *fabric evolution is path-dependent*. Li and Dafalias [26] and Gao et al. [15] provide some specific discussions on this topic.

3.5. Signature of anisotropy at characteristic states

The three characteristic states studied here have both theoretical significance and practical importance. Defining the critical state has been the cornerstone of critical state soil mechanics. The phase transformation and liquefaction states have been closely discussed with regard to various engineering failures [22]. This section discusses the characteristics signifying the three important states.

3.5.1. Phase transformation

The phase transformation state (PTS) marks a granular soil deformation changing from contractive behaviour to a dilative response. Under drained conditions, the PTS corresponds to $\delta\epsilon_v^p = 0$ in the loading course [21], whereas it manifests itself as $\delta p' = 0$ in the effective stress path under undrained conditions. The PTS is considered intrinsic [22]. To understand the micro-structural mechanism underpinning PTS occurrences, the evolution of the coordination number Z may offer helpful information. From Fig. 11 in conjunction with Figs. 3 and 4, we found that the PTS always marks a local extremum (either a peak or valley, marked by star symbols in Fig. 11) in the evolution of Z (see also [55]). Specifically, the PTS corresponds to a valley under undrained condition and a local peak under drained shear. The difference in the two drainage conditions is due to the constraint on volumetric change during the loading process. Though not particularly obvious, Fig. 13 also shows that the fraction of sliding contacts in all contacts approaches a peak when a PTS occurs.

3.5.2. Liquefaction

Liquefaction refers to the dramatic reduction of effective stress and shear strength in sand due to the fast buildup of excessive pore water pressure under undrained or partially drained loading conditions. Liquefaction has long been attributed to many engineering disasters, including debris flow and landslides. We first examine the internal structure when liquefaction occurs. Fig. 14 presents the contact force network in sample UL at the liquefaction state. Compared to those in Fig. 5, the entire force network in UL at liquefaction is extremely weak, with an average contact force of $\bar{f} = 0.003$ N, less than 10% of that at the phase transformation state for UM. The bimodal feature in this network also becomes less distinctive where no appreciable penetrating strong force chains are identifiable (the thickness of all chains in Fig. 14 have been scaled 15 times greater than in Fig. 5 for better visualisation, indicated in the different legends in these figures). The entire sample becomes so loose that no sufficient contacts can be established to sustain any shearing. Meanwhile, a certain proportion of contacts in the weak force subnetwork has been mobilised to orient slightly more in the vertical direction to share a small deviatoric force. This has also been verified by the anisotropy evolution in UL shown in Fig. 8a. Compared to other samples, a notable difference in UL is that a_c in Γ_{weak}, instead of staying approximately near zero, evolves steadily from a negative value to a positive value and reaches $a_c = 0.39$ at liquefaction. This indicates that in an extremely loose assembly, the weak contacts must share the deviatoric load with
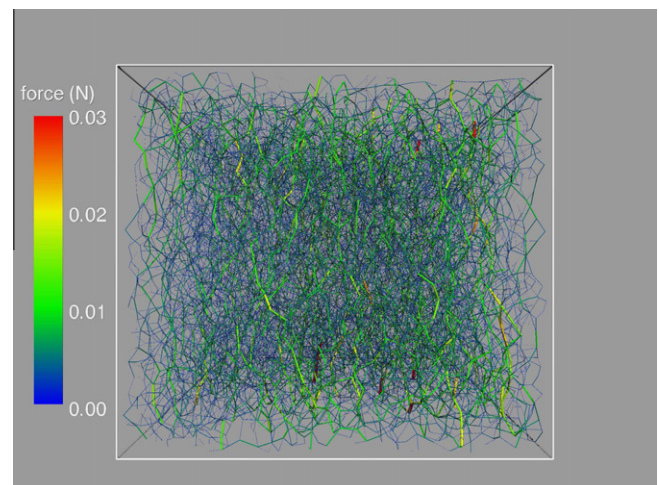

Fig. 14. Force chain network at liquefaction for sample UL ($\bar{f} = 0.003N$).

the strong contacts due to insufficient contacts. Fig. 11a indicates that both the coordination number and average contact force drop drastically during shearing before liquefaction. The reduction in contact number also greatly sacrifices the ability of the weak force network to act as the lateral prop for the strong contact force chains. The vertical strong force columns thus become fragile and are prone to buckling, which causes catastrophic failure modes such as liquefaction.

Fig. 7a also shows that the weight of a_c in the overall shear strength for UL increases rapidly and surpasses that of a_n at approximately 6% axial strain when liquefaction is impending. This implies that geometrical anisotropy at liquefaction dominates mechanical anisotropy, which is a unique characteristic for liquefaction. Considering the normal dominance of mechanical anisotropy in all the other cases, *mechanical anisotropy losing dominance to geometrical anisotropy can be considered the signature of anisotropy at liquefaction.*

The proportion of sliding contacts could serve as another indicator for liquefaction. Fig. 13 shows that the sliding contacts at the liquefaction state comprise over 40% of the total contacts in the assembly, while it comprises only approximately 15% in other cases. These sliding contacts are exclusively mobilised in the weak force network [42]. In conjunction with Fig. 12, the proportion of sliding contacts in the weak force network is roughly 0.4/0.62 = 65% in UL at liquefaction, while the proportion is only about 0.15/0.63 = 24% at the critical state in cases where liquefaction does not occur. A high fraction of sliding contacts in the weak force network (e.g., greater than 0.5) likely suggests a high risk of liquefaction.

3.5.3. Critical state

Critical state refers to a continuous flow state with constant mean effective stress, deviatoric stress and volume (void ratio) in a granular soil. Our DEM simulations indicate that all samples except UL reach a critical state at approximately 50% axial strain. These can be observed in Figs. 3 and 4 as well as Fig. 6, where a critical stress ratio $q/p' = 0.72$ is shown independent of the initial states or loading paths. While critical state is evidently anisotropic, as visualised in Fig. 5d, extra constraints pertaining to anisotropy must be added to the conventional critical state conditions to complete it. To gain further confidence, over 10 extra DEM tests have been performed on packings with different confining pressures and initial states and following drained/undrained loading paths. The obtained results are summarised below.
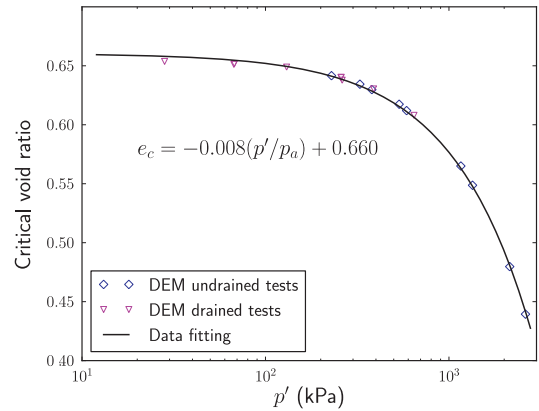
3.5.3.1. Critical void ratio.
With the added data points from the extra tests, Fig. 15a plots the correlation between the mean effective stress and critical void ratio. A linear p'-dependent critical state void ratio is observed[3]:

$$e_c = 0.66 - 0.008 \left(\frac{p'}{p_a} \right),$$

where p_a is the atmospheric pressure. The linear relation is consistent with experimental data on Erksak sand [7] and Toyoura sand [22], as well as the DEM results [34] using bidisperse ellipsoidal particles. Indeed, the observed linear relation obviously belongs to a bigger class of sand with the following power law form:

$$e_c = e_\Gamma - \lambda_e \left(\frac{p'}{p_a} \right)^\xi, \tag{14}$$

---

[3] The relation is linear in a normal $e - p'$ plot, but it is presented here in a semi-log plot to compare it to the following critical fabric anisotropy and follow the custom in soil mechanics in presenting the critical e–p' relation in a semi-log plot.

(a) critical void ratio
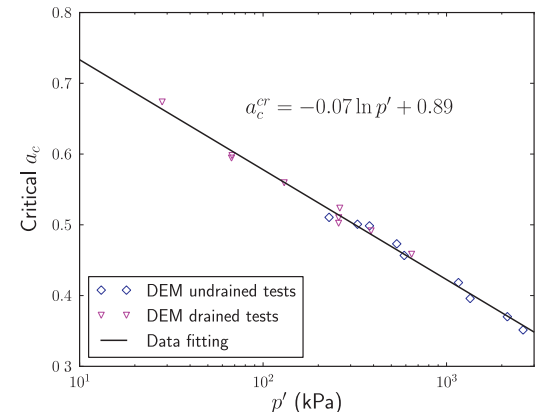
(b) critical fabric anisotropy

Fig. 15. Critical state lines of samples (p_a = 1 atm). Numerical data points are denoted by triangles and diamonds.

where e_Γ denotes the critical void ratio at $p' = 0$ and λ_e and ξ are material constants. Been et al. [7] have adopted a specific form $e_c = 0.9325 - 0.019(p'/p_a)^{0.7}$ to fit the critical void ratio with pressure for Toyoura sand well.

3.5.3.2. Critical fabric anisotropy.
A similar striking correlation between the critical fabric anisotropy a_c^{cr} and mean pressure has also been found, as in Fig. 15b, where a linear relationship exists between a_c^{cr} and $\ln p'$

$$a_c^{cr} = 0.89 - 0.07 \ln p'$$

Analogous to the critical void ratio, the above expression can be further extended to a more general form:

$$a_c^{cr} = a_\Gamma - \lambda_a \ln \left(\frac{p'}{p_a} \right), \tag{15}$$

where a_Γ denotes the critical fabric anisotropy at $p' = p_a$ and λ_a is a material parameter (both a_Γ and λ_a may vary with loading path, e.g., showing a dependence on the Lode angle, which requires further verification). Eq. (15) suggests that a linear dependence of the fabric change rate $\dot{a}_c$ on the p_{ref}/p' should be included in a fabric evolution law. p_{ref} denotes a reference pressure used only for normalising, which can adopt either the atmospheric pressure or some initial confining pressure.

The unique relationship between the critical fabric anisotropy and pressure provides an important critical state condition using fabric anisotropy. Including this condition, the classic critical state theory may offer a more complete description of critical state

behaviour. The results obtained here also provide a practical way for future constitutive granular media studies to consider fabric anisotropy. Realistic constitutive models for sand should include proper fabric anisotropy evolution laws that respect the relation in Eq. (15) as a reference ultimate state.

Summary 5. The phase transformation state corresponds to a local extremum in coordination number and a peak in the sliding contact proportion in the entire network. Liquefaction represents a state in which geometrical anisotropy dominates mechanical anisotropy with a high fraction of sliding contacts in the weak force network. The critical state should be defined using both the unique critical void ratio and unique critical fabric anisotropy.

4. Conclusions and discussion

A micromechanical study has been presented to investigate the signature features of anisotropy in granular material under shear. Based on DEM results from drained/undrained triaxial compression tests, the characteristics of anisotropy and its evolution as well as three characteristic states important to soil mechanics are carefully examined. Novel findings from the study are summarised below:

- The internal structure in a granular system evolves continuously during shearing and depicts a bimodal character in the contact force network. The weak network always shows an isotropic feature, while the nature of the whole network is dominated by that of the strong contact force network. A strongly anisotropic strong network always leads to an anisotropic internal structure for the entire sample.
- Our DEM results have verified an analytical stress-force-fabric relationship for both drained and undrained tests. The shear strength that a granular material may have is proportional to the degree of anisotropy it can develop. The mechanical anisotropy plays a dominant role in providing shear resistance in medium to dense samples.
- For medium to dense sands, mechanical and geometrical anisotropies evolve with shear strain similarly. The strong force network dominates the overall anisotropy evolution. Mobilising the mechanical anisotropy a_n and a_t is much quicker than mobilising a_c. Weak force contacts comprise a dominant proportion of the entire contact network, and sliding contacts constitute around 1/6 of all contacts during shearing. The coordination number evolution features an early local extremum before evolving to a steady critical state value, which is not unique.
- The phase transformation state corresponds to a local extremum in the coordination number and a peak in the sliding contact proportional throughout the entire network.
- Liquefaction represents a state in which geometrical anisotropy dominates mechanical anisotropy with a high fraction of sliding contacts in the weak force network.
- Critical state corresponds to a continuously flowing anisotropic fabric structure. In addition to a linear relation between critical void ratio e_c and p', a unique linear dependence of critical fabric anisotropy a_c^{cr} on $\ln p'$ is found. The p'-dependent relations of both e_c and a_c^{cr} offer a more complete reference for the critical state than the classic critical state theory.

The above findings may help improve our understanding on the behaviour of granular materials at the particle level and offer useful information on developing suitable constitutive relations for granular materials. The current study constitutes a first step towards developing statistical mechanics-based plasticity models

for granular materials, which bears some similarities to the concept of multiscale modelling or macro–micro bridging [52,27,3]. The signature behaviour of various characteristic states captured in the study may be used as controlling factors for developing physical-based evolutionary laws for anisotropy. Meanwhile, it is helpful to discuss the limitations of the current study and possible future improvements.

(a) All simulations and analyses in this paper have been based on triaxial compression simulations. To validate whether the above observations are general enough, further studies are required to explore the granular response to more complex loading paths, e.g., rotational shear and/or cyclic loading. Garciá and Medina [17] have reported switching between strong–weak network anisotropy for a granular assembly subjected to uniaxial cyclic loads. Under rotational shear, the principal stress directions change continuously. The fabric adjusts itself to be compatible with the stress in both magnitude and direction. As the adjustment cannot be fulfilled instantaneously, a non-coaxial property is expected, which results in a more contractive and softer behaviour of the material [28]. A similar behaviour is observed when both the stress ratio and principal stress directions change [49].

(b) This study has used spherical particles. All observations have been made on samples considering free particle rolling. Considering rolling resistance and/or using non-spherical particles may help account for more realistic particle kinematics. Considering rolling resistance has been shown to help increase material shear strength [12]. Ng [34] has employed bidisperse ellipsoidal particles and found a linear relationship between critical void ratio and mean effect stress similar to the present paper. While particle shape does not appear to significantly affect the critical void ratio, nonspherical particles may facilitate forming a strongly anisotropic force network and may likely influence anisotropy behaviour considerably. Indeed, 2D studies on particle shape [4] have shown that geometrical anisotropy may decrease while the mechanical anisotropy is greatly enhanced when using pentagons instead of circular disks. With particle shape influencing geometrical anisotropy, it remains to be explored if a linear relation between critical a_c and $\ln p'$ holds if nonspherical particles are used. Other than particle shape and rolling resistance, other factors may affect the behaviour of granular response in DEM simulations. Thornton [48] and Rothenburg and Kruyt [45] have shown that increasing interparticle friction can lead to an increased critical void ratio but to decreases in the percentage of sliding contact and coordination numbers at a critical state. Mollon and Zhao [33] have recently developed a new method of generating sand particles with realistic shape which may be used in the future to verify the conclusions made above.

(c) All samples used in the study have been sheared from an initially isotropic state. As such, the study is essentially limited to the case of *induced anisotropy*, as termed by some researchers [38,44]. A more appealing initial state for geotechnical engineers is one that has been anisotropically consolidated or one with *inherent anisotropy*. This may be verified in the future. However, given prolonged deformation, the shearing process may essentially demolish the initial fabric structure, which makes the critical state lose all memory of this initial fabric structure such that the above conclusions regarding critical state may remain valid. Because anisotropy evolution is path-dependent, inherent anisotropy may influence the phase transformation and/or liquefaction behaviour, as the deformation level that the

material reaches at the two states is not high enough. Thorough investigations in this regard are needed in the future. Using non-spherical particles would also help achieve packings that exhibit initial anisotropy (see, e.g., [13]).

Acknowledgements

References

[1] Abe S, Place D, Mora P. A parallel implementation of the lattice solid model for the simulation of rock mechanics and earthquake dynamics. Pure Appl Geophys 2004;161:2265–77.

[2] Alonso-Marroquin F, Luding S, Herrmann HJ, Vardoulakis I. Role of anisotropy in the elastoplastic response of a polygonal packing. Phys Rev E 2005;71:051304.

[3] Andrade J, Avila C, Hall S, Lenoir N, Viggiani G. Multiscale modeling and characterization of granular matter: from grain kinematics to continuum mechanics. J Mech Phys Solids 2010;59:237–50.

[4] Azéma E, Radjaï F, Peyroux R. Force transmission in a packing of pentagonal particles. Phys Rev E 2007;76(1):011301.

[5] Bagi K. Stress and strain in granular assemblies. Mech Mater 1995;22:165–77.

[6] Barreto D, O'Sullivan C. The influence of inter-particle friction and the intermediate stress ratio on soil response under generalized stress conditions. Granul Matter 2012;14(4):505–21.

[7] Been K, Jefferies MG, Hachey J. The critical state of sands. Géotechnique 1991;41(3):365–81.

[8] Cambou B, Dubujet P, Nouguier-Lehon C. Anisotropy in granular materials at different scales. Mech Mater 2004;36:1185–94.

[9] Chantawarungal K. Numerical simulations of three dimensional granular assemblies. Ph.D. thesis, University of Waterloo, Ontario, Canada, 1993.

[10] Christoffersen J, Mehrabadi MM, Nemat-Nasser S. A micromechanical description of granular material behavior. J Appl Mech 1981;48:339–44.

[11] Collins I, Muhunthan B. On the relationship between stress-dilatancy, anisotropy and plastic dissipation for granular materials. Géotechnique 2003;53(7):611–8.

[12] Estrada N, Taboada A, Radjaï F. Shear strength and force transmission in granular media with rolling resistance. Phys Rev E 2008;78(2):021301.

[13] Fu P, Dafalias Y. Fabric evolution within shear bands of granular materials and its relation to critical state theory. Int J Numer Anal Meth Geomech 2011;35:1918–48.

[14] Gao Z, Zhao J. Constitutive modeling of artificially cemented sand by considering fabric anisotropy. Comput Geotech 2012;41:57–69.

[15] Gao Z, Zhao J, Li X, Dafalias Y, 2012. A critical state sand plasticity model accounting for fabric evolution. Int. J. Plast. submitted for publication.

[16] Gao ZW, Zhao JD, Yao YP. A generalized anisotropic failure criterion for geomaterials. Int J Solids Struct 2010;47(22-23):3166–85.

[17] Garciá X, Medina E. Strong–weak network anisotropy switching and hysteresis in three dimensional granular materials. Phys Rev E 2008;78:021305.

[18] Goldenberg C, Goldhirsch I. Friction enhances elasticity in granular solids. Nature 2005;435:188–91.

[19] Guo N, Zhao J. Bimodal character of induced anisotropy in granular materials under undrained shear. In: Jiang M, Liu F, Bolton M, editors. Proceedings of the international symposium on geomechanics and geotechnics: from micro to macro. CRC Press-Taylor & Francis; 2010. p. 513–7.

[20] Gutierrez M, Ishihara K. Non-coaxiality and energy dissipation in granular material. Soils Found 2000;40:49–59.

[21] Ibsen LB, Lade PV. The role of the characteristic line in static soil behavior. In: Balkema AA, editor. 4th Workshop on localisation and bifurcation theory for soils and rocks, 1998. p. 221–30.

[22] Ishihara K. Liquefaction and flow failure during earthquakes. Géotechnique 1993;43(3):351–415.

[23] Johnson K. Contact mechanics. London: Cambridge University Press; 1985.

[24] Kuhn MR. Structured deformation in granular materials. Mech Mater 1999;31:407–29.

[25] Lade PV. Failure criterion for cross-anisotropic soils. J Geotech Geoenviron Eng 2008;134(1):117–24.

[26] Li X, Dafalias Y. Anisotropic critical state theory: the role of fabric. J Eng Mech 2012;138(1):263–75.

[27] Li X, Yu H, Li X. Macro–micro relations in granular mechanics. Int J Solids Struct 2009;46:4331–41.

[28] Li X, Yu H-S. Numerical investigation of granular material behaviour under rotational shear. Géotechnique 2010;60(5):381–94.

[29] Li XS, Dafalias YF. Constitutive modeling of inherently anisotropic sand behavior. J Geotech Geoenviron Eng, ASCE 2002;128(1):868–80.

[30] Mair K, Hazzard JF. Nature of stress accommodation in sheared granular material: insights from 3d numerical modeling. Earth Planet Sci Lett 2007;259:469–85.

[31] Majmudar TS, Behringer RP. Contact force measurements and stress-induced anisotropy in granular materials. Nature 2005;435(23):1079–82.

[32] Mitchell JK, Soga K. Fundamentals of soil behavior. 3rd ed. Chichester: John Wiley & Sons; 2005.

[33] Mollon G, Zhao J. Fourier-Voronoi-based generation of realistic samples for discrete modelling of granular materials. Granular Matter, in press. http://dx.doi.org/10.1007/s10035-012-0356-x.

[34] Ng T-T. Discrete element method simulations of the critical state of a granular material. Int J Geomech 2009;9(5):209–16.

[35] Oda M. Initial fabrics and their relations to mechanical properties of granular materials. Soils Found 1972;12:17–36.

[36] Oda M. Fabric tensor for discontinuous geological materials. Soils Found 1982;22(4):96–108.

[37] Oda M, Iwashita K. Mechanics of granular materials: an introduction. Brookfield (VT): A.A. Balkema; 1999.

[38] Oda M, Nemat-Nasser S, Konishi J. Stress-induced anisotropy in granular masses. Soils Found 1985;25:85–97.

[39] Ouadfel H, Rothenburg L. 'Stress–force–fabric' relationship for assemblies of ellipsoids. Mech Mater 2001;33:201–21.

[40] Radjaï F. Particle-scale origins of shear strength in granular media. In: Evolution, vol. 1. Van Nostrand Reinhold, 2008, p. ix, 290. <http://arxiv.org/abs/0810.4722>.

[41] Radjaï F, Troadec H, Roux S. Key features of granular plasticity. In: Antony SJ, Hoyle W, Ding Y, editors. Granular materials: fundamentals and applications. The Royal Society of Chemistry. Cambridge; 2004. p. 157–84.

[42] Radjaï F, Wolf DE, Jean M, Moreau JJ. Bimodal character of stress transmission in granular packings. Phys Rev Lett 1998;80:61–4.

[43] Rothenburg L. Micromechanics of idealized granular systems. Ph.D. thesis, Carleton University, Ottawa, Ontario, Canada, 1980.

[44] Rothenburg L, Bathurst RJ. Analytical study of induced anisotropy in idealized granular materials. Géotechnique 1989;39(4):601–14.

[45] Rothenburg L, Kruyt NP. Critical state and evolution of coordination number in simulated granular materials. Int J Solids Struct 2004;41:5763–74.

[46] Satake M. The role of the characteristic line in static soil behavior. In: Balkema AA, editor. IUTAM symposium on deformation and failure of granular materials, Delft; 1982. p. 63–8.

[47] Sitharam TG, Vinod JS, Ravishankar BV. Post-liquefaction undrained monotonic behaviour of sands: experiments and DEM simulations. Géotechnique 2009;59(9):739–49.

[48] Thornton C. Numerical simulations of deviatoric shear deformation of granular media. Géotechnique 2000;50(1):43–53.

[49] Thornton C. Quasi-static simulations of compact polydisperse particle systems. Particuology 2010;8:119–26.

[50] Thornton C, Antony SJ. Quasi-static deformation of particulate media. Philos Trans R Soc Lond A 1998;356(1747):2763–82.

[51] Tordesillas A, Muthuswamy M. On the modeling of confined buckling of force chains. J Mech Phys Solids 2009;57:706–27.

[52] Tordesillas A, Walsh SDC, Gardiner BS. Bridging the length scales: micromechanics of granular media. BIT Numer Math 2004;44:539–56.

[53] Voivret C, Radjaï F, Delenne J, El Youssoufi M. Multiscale force networks in highly polydisperse granular media. Phys Rev Lett 2009;102:178001.

[54] Wang Y, Alonso-Marroquin F. A finite deformation method for discrete modeling: particle rotation and parameter calibration. Granul Matter 2009;11:331–43.

[55] Yang J, Dai BB. Is the quasi-steady state a real behaviour? A micromechanical perspective. Géotechnique 2010;61(2):175–83.

[56] Yimsiri S, Soga K. DEM analysis of soil fabric effects on behavior of sand. Géotechnique 2010;60(6):483–95.

[57] Yoshimine M, Ishihara K, Vargas W. Effects of principal stress direction and intermediate principal stress on undrained shear behavior of sand. Soils Found 1998;38(3):179–88.

[58] Zhao J, Guo N. Signature of anisotropy in liquefiable sand under undrained shear. In: Bonelli S, Dascalu C, Nicot F, editors. Advances in bifurcation and degradation in geomaterials: Proceedings of the 9th international workshop on bifurcation and degradation in geomaterials, Vol. 11. Springer; 2011. p. 45–51.